IEEE Open Journal of the
Industrial Electronics Society

Received 27 January 2022; revised 4 March 2022; accepted 17 March 2022. Date of publication 12 April 2022;
date of current version 6 May 2022. The review of this paper was arranged by Associate Editor Giampaolo Buticchi.

Digital Object Identifier 10.1109/OJIES.2022.3163014

Highly Dynamic Eddy-Current-Based Sealed Magnetic Bearing Position Measurement With Temperature Drift Correction - "Seeing Through Conductive Walls"

ROSARIO V. GIUFFRIDA (Student Member, IEEE), SPASOJE MIRIĆ (Student Member, IEEE), JOHANN W. KOLAR (Fellow, IEEE), AND DOMINIK BORTIS (Senior Member, IEEE)

Power Electronic Systems Laboratory, ETH Zurich, 8092 Zurich, Switzerland

CORRESPONDING AUTHOR: ROSARIO V. GIUFFRIDA (e-mail: giuffrida@lem.ee.ethz.ch).

This work was supported by the Else und Friedrich Hugel-Fonds fur Mechatronik/ETH Foundation for the research on magnetically levitated systems at the Power Electronic Systems Laboratory of ETH Zurich.

ABSTRACT This paper investigates the design of an Eddy Current Sensor (ECS) for position measurement of a moving conductive target located behind a fixed conductive shielding surface. Such a sensor can e.g. be used in completely sealed actuators with magnetically levitated rotor or mover for high purity applications. Starting from the analysis of the sensor's operating principle, the design of the excitation coil, the achievable sensitivity and bandwidth as well as the temperature stability of the sensor are investigated. Subsequently, a suitable sensor interface, consisting of the driving and signal conditioning electronics, is selected. With this it is possible to distinguish between position and temperature variations, for which the optimal operational frequencies are identified. The results are finally verified with measurements on a hardware sensor prototype, showing that the ECS can achieve a sensitivity of 1 mV/µm, a position resolution of 1 µm, with a measurement bandwidth of 30 kHz and can hence be used to capture the mover's position in an active magnetic bearing feedback control structure.

INDEX TERMS Eddy Currents, Magnetic Levitation, Position Measurement.

I. INTRODUCTION

In many industrial applications a contactless position sensing of an object is of main importance. In the case of a conductive object, a popular choice are Eddy Current Sensors (ECSs), which due to their non-contact nature offer a clear advantage over e.g. resistive or capacitive sensors [1], [2]. Moreover, ECSs can also operate under harsh conditions, dirty environments or in vacuum, which makes them applicable for Magnetic Bearings (MBs) of magnetically levitated actuator systems [3]–[6], where the ECSs located on the stator are used to capture the position of the levitated mover (cf. Fig. 1(a)). ECSs are also extensively used in Non-Destructive Testing (NDT) for inspection of damages on the surface of conductive materials [7]. There are also applications where the moving conductive target is located behind another conductive material. For example, in entirely sealed actuator systems used for high purity food, medical or chemical applications, the stator and the magnetically levitated mover are fully encapsulated with e.g. a stainless steel housing (cf. Fig. 1(b)). Consequently, the ECS located on the stator has to measure the mover position through the stator housing, which due to its conductivity highly degrades the magnetic coupling between excitation and/or pick-up coil and the mover, and in turn leads to a reduction of the measurement sensitivity, i.e. the mover's position accuracy. As a further challenge, the sensor is expected to operate under different temperature conditions, as high as 100 °C due to ohmic losses in the stator. Therefore, it is important to study the sensor's stability with respect to temperature sensitivity, in order to prevent the magnetic bearings from failing due to thermal drift of the measured mover's position. In contrast to other magnetic sensors as e.g. Hall effect sensors, which can also be used to estimate

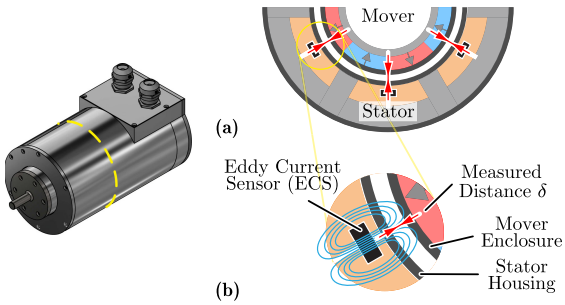

FIGURE 1. 3D-view of a magnetically levitated rotary-linear actuator system with (a) corresponding cross section showing the placement of the Eddy Current Sensors (ECSs) inside a sealed stator. (b) Detail of the sealed actuator with the used ECS, which has to measure the mover's position through the conductive stator housing.

TABLE 1 ECS Specifications Defined by the Underlying Application

Parameter	Value	Unit
Measurable Distance δ	$0 \ldots 2$	[mm]
Sensor Resolution	$1 \ldots 10$	[µm]
Sensor Bandwidth f_{bw}	> 10	[kHz]
Max. ECS Coil Diameter d_{c}	11.5	[mm]
Enclosure Thickness (Stator and Mover)	$0.2 \ldots 0.5$	[mm]
Enclosure Material (Stator and Mover)	Stainless Steel	

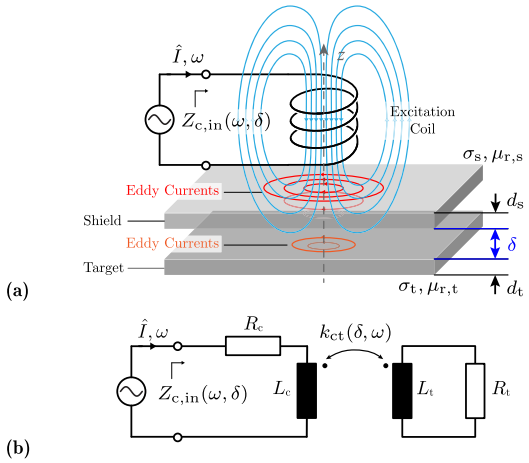

FIGURE 2. (a) Planar single-coil ECS measuring the distance δ between the stationary intermediate conductive shield and the moveable conductive target. (b) Transformer equivalent circuit for the conventional ECS (*without* intermediate shield) with coil and target self-inductances L_{c} and L_{t} as well as the frequency- and distance-dependent coupling factor $k_{\mathrm{ct}}(\omega, \delta)$.

the mover's position through the stator's housing exploiting the magnetic field of the mover's permanent magnets, ECSs typically provide higher resolution, thermal stability and immunity to external disturbing magnetic fields [2], [3]. In the literature [8], such an ECS measuring through a conductive wall is e.g. used for periodical inspections of nuclear power plants by measuring the distance between two conductive tubes. There, a commercial ECS is used, with excitation frequencies up to 16 kHz, which for stationary applications are clearly sufficient. However, for highly dynamic position measurements in entirely sealed MBs, this could result in a too low measurement bandwidth. For instance, in very-high-speed magnetically levitated machines, position control bandwidths up to 1 kHz are needed [9]. Consequently, sensor measurement bandwidths of at least 10 kHz have to be achieved [3], [5], which in turn roughly lead to 10 times higher excitation frequencies of about 100 kHz. Importantly, however, it has also to be considered that above a certain excitation frequency, defined by the material properties and dimensions of the conductive wall, the skin and proximity effects of this intermediate layer start to play an important role, leading in the worst case to a complete loss of any mover position information. Consequently, the ECS's excitation frequency has to be selected properly, such that on one hand a sufficient position sensor bandwidth is achieved and, on the other hand, the position sensitivity is not compromised too much by the intermediate conductive layer.

This paper extends the previous work of the authors [10], thoroughly presenting and discussing the design of an ECS capable of measuring through conductive walls. In particular, the ECS is used as a position sensor for entirely sealed actuator systems with a magnetically levitated mover, targeting the specifications of Table 1. After shortly summarizing the sensor's operating principle presented in [10] in Section II, in the first part of this work the modeling and optimal design of the excitation coil, i.e. the sensor head, is analyzed. More specifically, in Section III an equivalent transformer model is introduced, whose circuit elements (impedances) are calculated analytically depending on the coil geometry and material properties. Furthermore, the model is validated by comparison with FEM simulations and measurements on the optimally-designed excitation coil. Afterwards, in Section IV the temperature's influence on the coil impedance is investigated and quantified, in order to propose a method to measure and/or compensate it.

In the second part of this work, the practical problem of selecting a sensor interface with appropriate signal conditioning, which finally provides a measurable voltage signal, is addressed. This explicitly takes into account the temperature's influence on the sensor's output, finally providing a way of measuring both position and temperature as described in detail in Section V. The concept is verified in Section VI with a hardware sensor prototype on which experimental measurements are performed. Finally, Section VII concludes the paper.

II. SUMMARY OF PREVIOUS WORK

In [10], the authors investigate the ECS measuring through a conductive wall starting from the analysis of the conventional ECS and extending it to the new configuration of Fig. 2(a). An ECS is typically realized as a coil carrying a high frequency excitation current, which induces eddy currents in a conductive target. The secondary magnetic field generated by the circulating eddy currents couples with the excitation coil and finally affects its equivalent input impedance $Z_{\mathrm{c,in}}$. The variations of $Z_{\mathrm{c,in}}(\omega, \delta)$ depend on the chosen excitation frequency $\omega_{\mathrm{exc}} = 2\pi f_{\mathrm{exc}}$ and, most importantly, on the air gap δ, which is the *measurand*.

For a conventional ECS (*without* intermediate shield), a convenient way of describing the variations of $Z_{c,in}(\omega, \delta) = R_{c,in}(\omega, \delta) + j\omega L_{c,in}(\omega, \delta)$ is the *transformer model* in Fig. 2(b) and results analytically in:

$$R_{c,in}(\omega, \delta) = R_c + \frac{\omega^2 M_{ct}^2}{R_t^2 + \omega^2 L_t^2} R_t = R_c + R_{c,var}(\omega, \delta), \quad (1)$$

$$L_{c,in}(\omega, \delta) = L_c - \frac{\omega^2 M_{ct}^2}{R_t^2 + \omega^2 L_t^2} L_t = L_c + L_{c,var}(\omega, \delta), \quad (2)$$

where $M_{ct} = k_{ct}\sqrt{L_c L_t}$ is the mutual inductance between coil (c) and target (t), with the coupling factor $k_{ct}(\omega, \delta)$. In order to obtain significant variations in $R_{c,in}$ and $L_{c,in}$ with the air gap δ, the excitation frequency has to be selected above a *coupling-independent* angular cutoff frequency

$$\omega_{co} = 2\pi f_{co} = R_t/L_t, \quad (3)$$

which can be found as the frequency for which $R_{c,in}$ and $L_{c,in}$ experience half of their total variations

$$R_{c,var}(\omega \to \infty, \delta) = \left(\frac{M_{ct}}{L_t}\right)^2 R_t = k_{ct}(\omega, \delta)^2 L_c \omega_{co}, \quad (4)$$

$$L_{c,var}(\omega \to \infty, \delta) = -\left(\frac{M_{ct}}{L_t}\right)^2 L_t = -k_{ct}(\omega, \delta)^2 L_c. \quad (5)$$

When a second intermediate conductive shield is added, eddy currents are also induced in it, thus affecting the variations of $Z_{c,in}(\omega, \delta)$ i.e. the position sensitivity. A general understanding of the resulting effect on $Z_{c,in}(\omega, \delta)$ can be gained as follows. Considering the case where $\delta \to \infty$, i.e. when the target is far away. This corresponds to the conventional ECS with the shield acting like a target, and hence the same considerations as before apply, but now $\omega_{co,s} = 2\pi f_{co,s} = R_s/L_s$ is defined by the shield. When the target approaches the shield, it offers a parallel circulation path for the eddy currents, thus reducing the original R_s of the shield alone. The secondary-side resistance can be substituted by an equivalent resistance R_{eq}, which can be seen as some special target at some equivalent position having mixed material properties of shield and target. The resulting R_{eq} is smaller than R_s and continuously reduces with the target approaching the shield. Consequently, also the cutoff frequency $\omega_{co,s}$ shifts to lower frequencies. For the extreme case with $\delta = 0$ mm, assuming that shield and target have the same coupling to the coil, the minimum cutoff frequency is roughly given by the parallel connection of R_s and R_t as

$$\omega_{co,min} = 2\pi f_{co,min} = R_s R_t/(R_s + R_t)/L_s. \quad (6)$$

This air gap-dependent shift of the cutoff frequency affects the variations of resistance $R_{c,var}$ and inductance $L_{c,var}$ as shown in the exemplary curves of Fig. 3, obtained with FEM simulations in [10] for different shield/target material combinations.

In particular, $L_{c,var}$ is mostly sensitive to variations of the air gap δ in the frequency range between $f_{co,min}$ and $f_{co,s}$ and, as derived in [10], the optimal excitation frequency $f_{opt,L}$ that maximizes the position sensitivity of $L_{c,var}$, lies approximately in the center of this interval, i.e. the geometric mean of the two

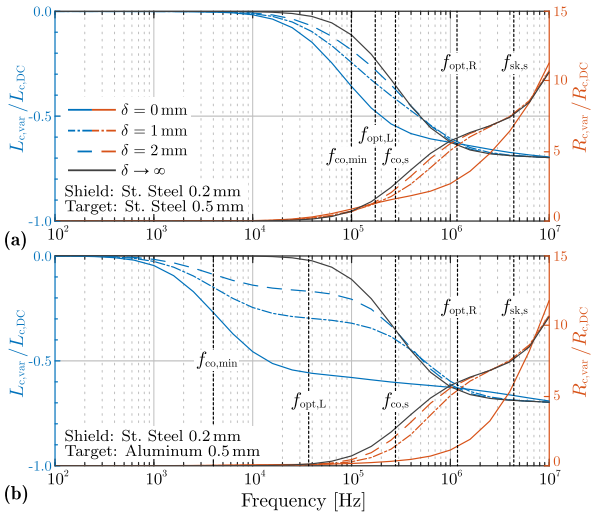

FIGURE 3. Normalized $R_{c,var}(\omega, \delta)$ and $L_{c,var}(\omega, \delta)$ versus frequency for (a) stainless steel/stainless steel and (b) stainless steel/aluminum shield/target combinations at $\delta = 0$ mm, 1 mm, 2 mm and $\delta \to \infty$ (shield only), obtained with FEM simulations. In this exemplary case, the resulting DC coil parameters are $R_c = 2.8\,\Omega$ and $L_c = 13.9\,\mu$H. The cutoff frequency f_{co}, the skin depth related frequency of the shield $f_{sk,s}$ and the optimal excitation frequencies $f_{exc,opt,R}$ and $f_{exc,opt,L}$ are also indicated.

boundary frequencies

$$f_{opt,L} \approx \sqrt{f_{co,min} \cdot f_{co,s}}. \quad (7)$$

The cutoff frequency shift also reduces the total resistance variation, as it appears from (4). Therefore, the frequency range for which $R_{c,var}$ is mostly sensitive to variations of δ lies above $f_{co,s}$. Nevertheless, in order to ensure that the excitation field penetrates the shield and eddy currents are induced in the target, the excitation frequency must be kept below a certain *skin-depth-related* frequency

$$f_{sk,s} = \frac{1}{\pi \mu_0 \mu_{r,s} \sigma_s d_s^2}, \quad (8)$$

where μ_0 is the magnetic permeability of vacuum and $\mu_{r,s}$, σ_s and d_s are the relative permeability, conductivity and thickness of the shield, respectively. In this work, only non-magnetic materials ($\mu_{r,\{s,t\}} = 1$) are considered. As it appears from (8), ferromagnetic materials (such as ferritic stainless steel) would reduce the penetration depth of the excitation field, resulting in lower sensitivity. Beyond $f_{sk,s}$, no sensitivity to δ can be achieved. Thus, the optimal excitation frequency $f_{opt,R}$, lies approx. in the center between $f_{co,s}$ and $f_{sk,s}$, i.e. again the geometric mean

$$f_{opt,R} \approx \sqrt{f_{sk,s} \cdot f_{co,s}}. \quad (9)$$

With these results, the authors provide some general design guidelines for the ECS measuring through conductive walls and identify the optimal excitation frequencies:

- In order to achieve a high measurement sensitivity, for both resistance and inductance variations, the shield resistance R_s should be much larger than the target resistance R_t, which is either obtained by selecting different materials or by using different thicknesses.

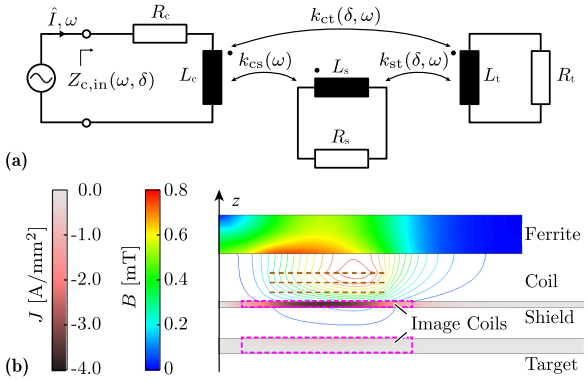

FIGURE 4. **(a) Extended transformer model with a secondary and a tertiary side modeling the equivalent input impedance $Z_{c,in}(\omega, \delta)$ of the excitation coil of the ECS measuring through conductive walls. The electric behavior of shield and target is described by the lumped secondary parameters $R_{\{s,t\}}$ and $L_{\{s,t\}}$ and the magnetic coupling between excitation coil, shield and target are considered by the three coupling factors k_{cs}, k_{ct} and k_{st}. (b) Axisymmetrical 2D FEM simulation (ANSYS Maxwell) with exemplary field and current distribution for a 0.2 mm stainless steel shield and 0.5 mm stainless steel target combination at an excitation frequency of $f_{exc} = 1.25$ mm. The shield and target image coils are highlighted in purple. A ferrite disk is added on top of the excitation coil to increase its self-inductance L_c.**

- A large shield resistance R_s increases both the cutoff frequency $f_{co,s}$ and the skin-depth-related frequency $f_{sk,s}$, resulting in a larger measurement bandwidth.
- The resistance variation starts around $f_{co,s}$ and ends around $f_{sk,s}$, which are both defined only by the shield layer.
- The range of inductance variation is defined by $f_{co,min}$ and $f_{co,s}$.
- The optimal excitation frequencies are roughly calculated with the geometric mean of the frequency boundaries.

These considerations were verified in [10] with measurements on a first hardware prototype for different material combinations.

III. ANALYSIS OF THE ECS MEASURING THROUGH WALLS

In [10] only the relations between $R_{c,var}(\omega, \delta)$, $L_{c,var}(\omega, \delta)$ and the optimal excitation frequencies were provided, but not how to calculate them for a given ECS configuration based on its electrical and geometrical parameters. The missing link is now added here, which makes it possible to optimally design the excitation coil of the ECS measuring through conductive walls and immediately estimate the position sensitivity. Furthermore, in case of an additional intermediate layer, the impedance variations of the excitation coil can be modeled analytically with an extended three-windings transformer model.

A. EXTENDED EQUIVALENT TRANSFORMER MODEL

In order to account for the additional shield layer, the transformer model previously introduced in Fig. 2(b) for the conventional ECS is extended as shown in Fig. 4(a), i.e. with a secondary side consisting of the series connection of the lumped shield resistance and inductance R_s and L_s and a tertiary side with the lumped target parameters. Consequently, also the mutual inductances $M_{cs} = k_{cs}\sqrt{L_c L_s}$ and $M_{st} = k_{st}\sqrt{L_s L_t}$ are introduced, where $k_{cs} = k_{cs}(\omega, \delta)$ and $k_{st} = k_{st}(\omega, \delta)$ are the coil-shield and shield-target coupling factors. It can be observed that k_{cs} is always larger than k_{ct}. By circuital analysis, an expression for the input impedance of the excitation coil $Z_{c,in}(\omega, \delta)$ can be provided. This is slightly more complicated with respect to the conventional ECS case, cf. (1) and (2), and is hence reported in the Appendix. The description of $Z_{c,in}$ provided by the transformer model is completed with the analytical expressions for all its parameters as derived in the following:

1) EXCITATION COIL (PRIMARY-SIDE) PARAMETERS

Expressions for the coil resistance R_c and inductance L_c can usually be found in the literature for different coil geometries [11], [12]. A common choice for ECSs is a PCB-integrated *planar spiral coil*, as it allows to obtain a relatively large inductance already with a single-layer coil. This allows to minimize the inter-layer parasitic capacitance of the coil, thus allowing to use higher excitation frequencies. Minimizing the parasitic capacitance $C_{c,par}$ is needed to guarantee that the coil's Self-Resonant Frequency (SRF) is well above the chosen excitation frequency. This is a stringent requirement for the correct operation of the ECS and the validity of the introduced transformer model. For the scope of this analysis it is sufficient to consider at least the following relations linking the coil geometry to its electrical properties. For the coil's DC resistance

$$R_c \propto \frac{d_{c,avg}\, N}{\sigma_{cu}}, \tag{10}$$

whereas for the inductance, in general

$$L_c \propto \mu_0\, d_{c,avg}\, N^2 \tag{11}$$

where $d_{c,avg}$ is the average diameter of the excitation coil.

2) SHIELD/TARGET (SECONDARY-SIDE) PARAMETERS

Providing expressions for the lumped shield or target resistance $R_{\{s,t\}}$ and inductance $L_{\{s,t\}}$ requires some preliminary consideration on the geometry of the eddy current circulation paths. Following [13], for a circular excitation coil the volume of the target carrying significant eddy currents (the *effective* volume) can be segmented into a certain number K of concentric rings. Each of them can be considered insulated with respect to the other, as it can be shown that the current density vector field $\vec{J}$ inside the target, expressed in polar coordinates, has no radial component. The simplest approximation, corresponding to $K = 1$, is to describe the effective volume with a circular single-turn *image coil* of rectangular cross section, with inner and outer radii r_{in} and r_{out}, as indicated in purple in Fig. 4(b). The thickness of such image coil can be assumed to be equal to the shield or target thickness $d_{\{s,t\}}$, as long as the eddy currents penetrate the material completely. However, for higher frequencies, the penetration depth reduces due to the well-known *skin effect*, according to the expression for the

skin depth

$$\delta_{\mathrm{sk},\{\mathrm{s,t}\}}(\omega) = \sqrt{\frac{2}{\mu_0 \mu_{\mathrm{r},\{\mathrm{s,t}\}} \sigma_{\{\mathrm{s,t}\}} \omega}} \tag{12}$$

When eventually $\delta_{\mathrm{sk},\{\mathrm{s,t}\}}$ becomes smaller than $d_{\{\mathrm{s,t}\}}$, the eddy currents are distributed only in a portion of the total shield or target thickness. Consequently, the effective height of the image coil is

$$h_{\{\mathrm{s,t}\}}(\omega) = \begin{cases} d_{\{\mathrm{s,t}\}}, & \text{for } \delta_{\mathrm{sk},\{\mathrm{s,t}\}}(\omega) \geq d_{\{\mathrm{s,t}\}} \\ \delta_{\mathrm{sk},\{\mathrm{s,t}\}}(\omega), & \text{otherwise} \end{cases} \tag{13}$$

which decreases for higher frequencies. However, a reduction of the penetration depth is only allowed for the target. The excitation frequency f_{exc} should always be lower than the skin-depth frequency of the shield. Consequently, thickness and the selected material of the shield immediately limit the excitation frequency range and the analysis thereof.

This way, $R_{\{\mathrm{s,t}\}}$ and $L_{\{\mathrm{s,t}\}}$ can be found as the resistance and the self-inductance of the respective equivalent image coil. For the resistance $R_{\{\mathrm{s,t}\}}$, it is sufficient to integrate the resistance of an infinitely thin loop in the volume of the image coil, obtaining

$$R_{\{\mathrm{s,t}\}}(\omega) = \frac{2\pi}{\sigma_{\{\mathrm{s,t}\}}\, h_{\{\mathrm{s,t}\}}(\omega)\, \ln\left(\frac{r_{\mathrm{out}}}{r_{\mathrm{in}}}\right)}. \tag{14}$$

For the inductance $L_{\{\mathrm{s,t}\}}$, instead, the empirical formula from [14] for a circular coil of rectangular cross section can be used

$$L_{\{\mathrm{s,t}\}}[\mu\mathrm{H}] \approx \frac{40\, r_{\mathrm{avg}}^2}{8\, r_{\mathrm{avg}} + 11\, (r_{\mathrm{out}} - r_{\mathrm{in}})}, \tag{15}$$

where $r_{\mathrm{avg}} = (r_{\mathrm{out}} + r_{\mathrm{in}})/2$ is the average radius of the image coil. In a first approximation, r_{in} and r_{out} can coincide with the inner and outer radii of the excitation coil, and hence $r_{\mathrm{avg}} = d_{\mathrm{c,avg}}/2$. In this case, FEM simulations reveal that 80% of the eddy currents are induced in this volume for both shield and target. The volume enclosed by an image coil with the same average radius r_{avg} but a 50% wider cross section (i.e. $1.5 \cdot (r_{\mathrm{out}} - r_{\mathrm{in}})$, as the ones represented in Fig. 4(b)) would instead consider up to 95% of the total eddy currents.

3) COUPLING FACTORS

Finally, the coupling factors can be obtained from the mutual inductances M_{cs}, M_{st} and M_{ct} according to the formula $k_{12} = M_{12}/\sqrt{L_1 L_2}$. With the introduced image coils, it is possible to use formulas for the mutual inductance of coaxial disk coils that can be found in the literature [15], [16]. As the model is highly sensitive to these three parameters, it is recommended to obtain or verify them with a FEM simulation.

B. OPTIMAL PCB-EMBEDDED COIL DESIGN CONSIDERATIONS

Once the transformer model and all the expressions for its parameters are introduced, they can be used to optimally design the excitation coil. As mentioned, this is typically realized as a PCB- or flex-PCB-embedded spiral coil, hence there are only a few main parameters to be determined, i.e. the coil diameter d_{c} and the number of turns N, which can be distributed in m layers. The optimal design procedure is summarized with the flow diagram of Fig. 5. The specified shield material with its conductivity σ_{s} and thickness d_{s} defines the skin-depth related frequency $f_{\mathrm{sk,s}}$ (cf. (8)). From the required controller bandwidth, the needed excitation frequency f_{exc} is defined, which coincides with $f_{\mathrm{opt,R}}$. Based on (9), it is hence possible to calculate the shield crossover frequency $f_{\mathrm{co,s}}$, which gives the ratio between R_{s} and L_{s} (cf. (3)). These two electrical parameters allow to select the dimensions of the image coil (average, inner and outer radii r_{avg}, r_{in} and r_{out}, cf. (14) and (15)) and, consequently, of the excitation coil. With the maximum diameter d_{c}, the maximum number of turns N of the excitation coil can be calculated, which gives a high excitation coil's self-inductance L_{c} and, in turn, a high position sensitivity (cf. (4) and (5)). The number of turns N can be further increased by using multiple PCB layers, but special care must be taken, as this particularly increases the parasitic capacitance $C_{\mathrm{c,par}}$, thus lowering the coil's SRF. Another way of further increasing L_{c}, compatibly with the available space in the stator, is to place a layer of ferromagnetic material on top of the excitation coil. As an additional benefit, this provides shielding against external disturbing magnetic fields.

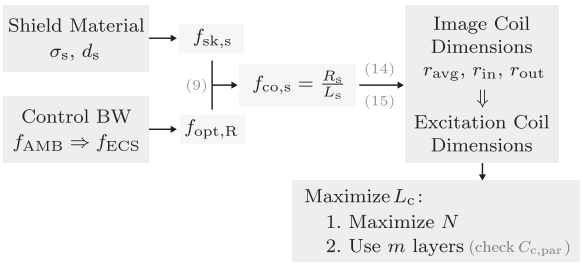

FIGURE 5. Flow diagram illustrating the optimal PCB-embedded coil design. From the specified shield material and control bandwidth, it is possible to define the characteristic frequencies, which are linked to the coil's geometry through the secondary-side parameters R_{s} and L_{s}. Once the coil's dimensions are obtained, its self-inductance L_{c} is maximized.

Therefore, for the given case, the excitation coil's diameter is maximized to the available $d_{\mathrm{c}} = 11.5\,\mathrm{mm}$, which with the minimum track width and distance of 150 µm yields a maximum number of turns per layer of $N = 13$. A picture of the realized PCB-embedded excitation coil is shown in Fig. 6(a). In order to ensure that the coil's SRF is above 10 MHz, (i.e. well above the range of the considered excitation frequencies), the number of PCB layers is limited to $m = 3$. In addition, a high-frequency ferrite core is added on top of the coil (cf. Fig. 6(b)) to further increase L_{c}, resulting in a total $L_{\mathrm{c}} = 13\,\mu\mathrm{H}$.

C. EXPERIMENTAL IMPEDANCE MEASUREMENTS AND MODEL VERIFICATION

The impedance variations of the ECS measuring through conductive walls are verified with the realized PCB-embedded excitation coil in the studied planar geometry of Fig. 2(a). This is realized with a collection of square samples of aluminum

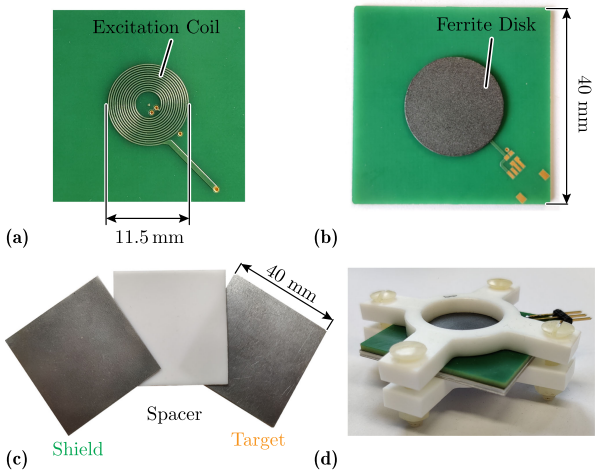

FIGURE 6. **(a) Realized PCB-embedded excitation coil. (b) On top of the excitation coil, a high-frequency ferrite disk is added to increase the self-inductance L_c. (c) Realized exemplary shield/target and spacer samples, made of stainless steel or aluminum and PTFE, respectively. (d) PCB coil buildup implementing the studied planar geometry, held together by a PTFE fixture.**

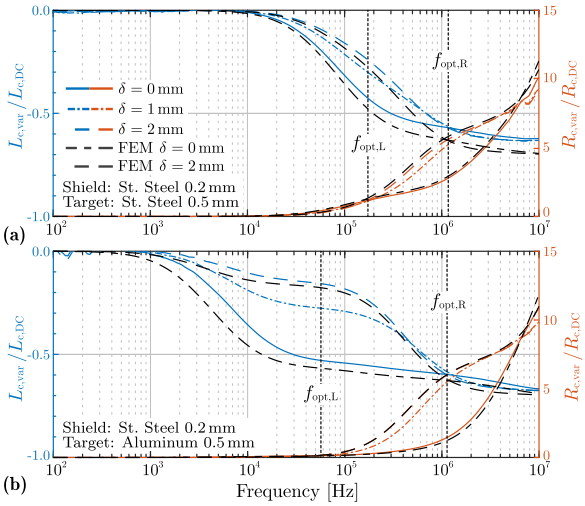

FIGURE 7. **Normalized $R_{c,var}(\omega, \delta)$ and $L_{c,var}(\omega, \delta)$ versus frequency for (a) 0.2 mm thick stainless steel shield and 0.5 mm thick stainless steel target configuration and (b) 0.2 mm thick stainless steel shield and 0.5 mm thick aluminum target configuration at $\delta = 0$ mm, 1 mm and 2 mm, as obtained from impedance measurements. For a direct comparison, also the FEM results for the cases $\delta = 0$ mm, 2 mm are reported (black dashed lines) and the optimal frequencies are indicated and reported in Table 2.**

and stainless steel (304, IE 1.4301, austenitic) with thicknesses 0.5 mm and 0.2 mm, to be used as shield or target (cf. Fig. 6(c)). The air gap between the two samples is fixed with spacers, realized with a non-conductive, temperature-resistant material (PTFE) and different thicknesses. This way, it is possible to fix the air gap in steps of 0.25 mm, which is the thickness of the thinnest spacer. The selected shield sample, spacer(s) and target sample are stacked up, with the excitation coil PCB on top, as shown in Fig. 6(d). All layers are also pressed together, thus reducing the bending of the metallic samples or the spacers. This measure is important to ensure correct results, especially considering the high sensitivity and the targeted resolution in the µm range.

The measurements are performed with the *Omicron Lab Bode100* impedance analyzer for the 0.2 mm thick stainless steel shield and 0.5 mm thick stainless steel target configuration and for the 0.2 mm thick stainless steel shield and 0.5 mm thick aluminum target configuration. The results are compared to the corresponding FEM simulations in Fig. 7, showing good agreement between the two. In particular, the optimal frequencies reported in Table 2 match closely. Also the values calculated with the analytical transformer model are reported and matching. The model allows to obtain the complete impedance curves, which however were found to be in agreement only until around $f_{sk,s}$. For the sake of this analysis and the optimal coil design, calculating the characteristic frequencies is sufficient, and therefore the impedance curves are not reported.

IV. TEMPERATURE'S INFLUENCE ON THE SENSOR'S OUTPUT

An important aspect to investigate for many sensors and particularly for the studied ECS is its behavior under different operating temperatures. Ideally, for a constant position, the

TABLE 2 **Comparison of the Optimal Excitation Frequencies**

	Fig. 7 (a)		Fig. 7 (b)		
	$f_{opt,L}$	$f_{opt,R}$	$f_{opt,L}$	$f_{opt,R}$	Unit
Measured	178	1189	56	1259	[kHz]
FEM	178	1122	47	1334	[kHz]
Analytical	175	1195	40	1195	[kHz]

sensor output has to stay constant throughout the entire range of operating temperatures. In the considered case, this problem is of particular interest. In fact, the temperature inside the sealed stator (where the ECS is located) varies in the range of 25 °C to 100 °C, since the actuator's winding, located inside the stator, heats up during operation. Consequently, a thermal drift of the sensor's output in active magnetic bearings would translate in a certain offset in the controlled position of the levitated mover with respect to the geometric center of the machine, which can lead in the worst case to failure of the levitation control. For these reasons, it is important to quantify the effect of temperature on the sensor's output and, possibly, take specific actions to limit or compensate it.

As a starting point for this investigation, it should be considered that the conductivity σ exhibits a temperature dependency. Another effect is thermal expansion, which however is not expected to be prominent in this case for thin shields or targets and is therefore neglected. As a consequence of the dependency on the conductivity σ, it has to be expected that the electrical properties of all the elements in the studied ECS configuration, i.e. coil, shield and target, are affected by temperature. The temperature dependency is usually given for the resistivity $\rho = \sigma^{-1}$ with the approximated linear relationship

$$\rho(T) = \rho_0 \left[1 + C_T (T - T_0)\right], \tag{16}$$

TABLE 3 Conductivity and Temperature Coefficient of the Considered Materials

Material	Conductivity at 25 °C σ_0	Temperature Coeff. (C_T)
Copper	59.6 MS	3900 ppm/°C
Aluminum	37.7 MS	3800 ppm/°C
Stainless Steel	1.37 MS	850 ppm/°C

where T is the temperature, ρ_0 is the resistivity of the material at the reference temperature T_0 (e.g. 25°C) and C_T is the *temperature coefficient* of the material, expressed in $°C^{-1}$. The values of ρ_0 and C_T for copper, aluminum and stainless steel are reported in Table 3. For the considered operating temperature range of 75°C, the resistivity of copper increases by about 30%.

Based on the analytical model previously introduced in Section III, it is already possible to predict qualitatively how the temperature influences $Z_{c,in}$. The most prominent effect, given the high C_T of copper, is the increase of R_c (cf. (10)), which offsets the total $R_{c,var}$ with respect to the nominal DC resistance at 25°C $R_{c,DC[25\,°C]}$. Secondly, also R_s and R_t increase with temperature (cf. (14)), according to their materials' properties. This reflects into an increase of the cutoff frequencies $f_{co,s}$ (cf. (3)) and $f_{co,min}$ (cf. (6)), which can affect the final sensitivity (cf. (4)) and alters the optimal excitation frequencies. Some influence has also to be expected for higher frequencies, as the skin depth $\delta_{sk,s}$ depends on σ_s as well. On the contrary, no relevant effect has to be expected on L_c (cf. (11)) nor on $L_{c,var}$ (cf. (5)). This is the main reason why conventional ECSs rely on $L_{c,var}$ to measure δ and disregard $R_{c,var}$ [17].

These considerations are verified by measuring the impedance of the realized PCB-integrated excitation coil at 25°C and 100°C. The measurements are conducted for the shield/target combination with 0.2 mm thick stainless steel shield and 0.5 mm thick stainless steel target, as well as 0.2 mm thick stainless steel shield and 0.5 mm thick aluminum target. The latter are shown in Fig. 8. With these results, it is possible to observe and quantify the influence of temperature on the equivalent input impedance of the excitation coil. As expected, this is much more prominent on $R_{c,in}$, with variations of about 30% of the value of $R_{c,DC[25°C]}$ at the optimal excitation frequencies, compared to $L_{c,in}$, which differs by less than 6% of the value of $L_{c,DC[25°C]}$ and is hence negligible. In particular, the increased DC resistance of the sensing coil R_c represents the main difference component of $R_{c,var}$, which is about 30% larger for all frequencies (cf. Fig. 8(b)). Additionally, the crossover frequencies $f_{co,min}$ and $f_{co,s}$ are shifted slightly towards higher frequencies as a result of the increased R_s and R_t, causing the largest differences in $L_{c,var}$ in Fig. 8(b). The prominent effect of temperature on $R_{c,var}$ leads to an error in the measured position, which can be visualized in Fig. 8(c) for different values of the air gap δ when exciting the coil at e.g. $f_{opt,R}$. If the sensor is calibrated for $T = 25°C$, in the extreme case of $T = 100°C$ the error δ_{err} on the measured position can be as large as 1.1 mm. This is

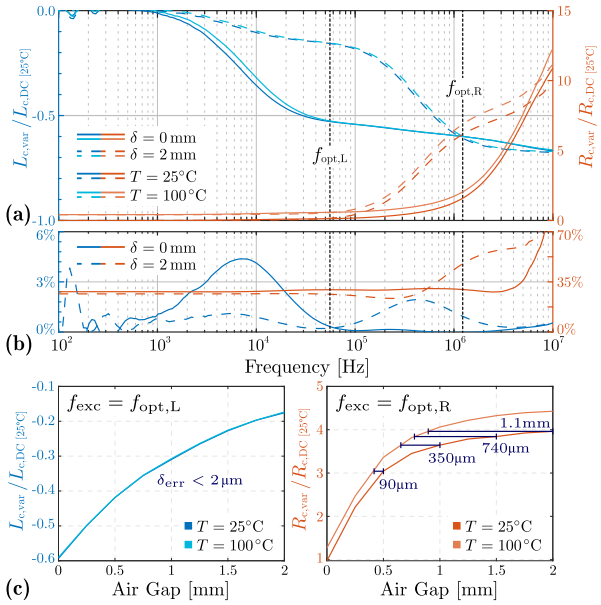

FIGURE 8. (a) Normalized $R_{c,var}(\omega, \delta)$ and $L_{c,var}(\omega, \delta)$ versus frequency for the 0.2 mm thick stainless steel shield and 0.5 mm thick aluminum target configuration at $\delta = 0$ mm and 2 mm and $T = 25°C$ and 100°C, as measured from the realized excitation coil. All values are normalized to its DC resistance and inductance at 25°C. (b) Differences between the normalized $R_{c,var}(\omega, \delta)$ and $L_{c,var}(\omega, \delta)$ at $T = 25°C$ and 100°C, for both $\delta = 0$ mm and 2 mm. The values represent the percent difference in $R_{c,var}(\omega, \delta)$ and $L_{c,var}(\omega, \delta)$ over $\Delta T = 75°C$. (c) Values of $R_{c,var}$ and $L_{c,var}$ versus air gap δ for $T = 25°C$ and 100°C, measured for the optimal inductance and resistance excitation frequencies. The position error δ_{err} due to the temperature variation $\Delta T = 75°C$ is indicated.

quite concerning for the stability of the magnetic bearings and needs to be explicitly corrected. On the other hand, if the same is checked for $L_{c,var}$ at the optimal excitation frequency $f_{opt,L}$, δ_{err} results smaller than 2 µm, i.e. temperature does not have a significant influence on the measured position. However, it has to be considered that $f_{opt,L}$ is smaller than $f_{opt,R}$, even by an order of magnitude in the case of Fig. 8(a), and it might not be sufficient for highly dynamic applications as e.g. very-high-speed magnetically levitated machines. In such a case, it is therefore necessary to be able to distinguish between impedance variations caused by position or temperature variations. This is only possible if full knowledge about the impedance $Z_{c,in}$ is gained, which means that not only $R_{c,in}$ or $L_{c,in}$ but both values have to be determined. In order to achieve this, an appropriate sensor interface is needed, as discussed in the next section. There it is shown that in this way, the ECS measuring through conductive walls allows to measure accurately the air gap δ, since variations in temperature T are compensated.

V. SENSOR INTERFACE AND SIGNAL CONDITIONING

Once the sensor concept is analyzed, it is possible to understand its operating principle and which quantities contain information on the measurand. The next problem to address is how to extract such information and convert it into a usable signal. For this purpose, a *measurement circuit* (or *sensor*

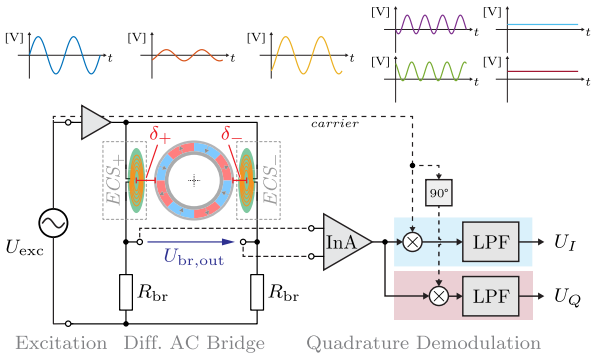

FIGURE 9. Schematic of the proposed measurement circuit, comprising excitation stage, differential AC Wheatstone bridge, amplification and demodulation stages. Differential sensing is realized by using two copies of the designed PCB-integrated excitation coil. In order to implement quadrature demodulation, two channels consisting each of a multiplier followed by a low-pass filter (LPF) are needed, together with a 90° carrier phase-shifter. Exemplary intermediate signals are also reported.

interface) is needed, which has three main functions. First, it has to provide an appropriate AC excitation signal to the sensor coil. Secondly, it has to transduce its impedance variations into measurable voltage or current signals. Finally, the obtained signals have to be further conditioned to be easily measured, e.g. to be digitized and acquired by a MCU and to be translated into a position. As mentioned, in the considered case an important requirement is the possibility of gaining full information on the excitation coil's impedance variation $\Delta Z_{c,in}(\delta, T, \omega)$, in order to be able to distinguish and measure both variations of the air gap δ and of the temperature T.

A. OVERVIEW OF THE PROPOSED MEASUREMENT CIRCUIT

An overview of the proposed measurement circuit is given in Fig. 9. It consists of three main parts, which implement the three aforementioned functions.

The excitation frequency $\omega_{exc} = 2\pi f_{exc}$ directly determines the sensor's position (and temperature) sensitivity, as it affects the penetration depth of the primary magnetic field in the shield-target combination. Therefore, it is reasonable to select a measurement circuit which operates with a *fixed* excitation frequency. Consequently, measurement circuits that perform an impedance-to-frequency conversion, commonly used for conventional ECS [18], have to be excluded. With a fixed excitation frequency, $\Delta Z_{c,in}$ can then be converted into an amplitude variation ΔU or ΔI.

The most suitable candidate circuit performing such conversion is the AC Wheatstone bridge, often found in the literature as an ECS interface [19]. The bridge is excited by a sinusoidal voltage signal U_{exc} with frequency f_{exc} and its output is the voltage $U_{br,out}$. This circuit is particularly well suited to measure unbalances between the impedances of its two legs. Therefore, in many cases, the excitation coil of the ECS is included in the bridge together with a replica, purposely manufactured and used as a *reference coil*, kept in nominal conditions (e.g at the nominal distance from the target). This solution is used for high precision sensors, capable e.g. to measure in the subnanometer range [20]. An additional advantage, in fact, is that any changes which are common to both coils (like e.g. the offset in R_c due to temperature found in Fig. 8), are canceled. In the considered application, due to the axial symmetry of the machine, it is advantageous to implement the ECS as a *differential sensor*, which is obtained by placing two identical copies of the excitation coil ECS_+ and ECS_- at the two opposite sides of the levitated rotor. By including both sensing coils in the AC Wheatstone bridge, it can be shown that the output voltage $U_{br,out}$ depends of the differential impedance $Z_{diff} = Z_{c+,in} - Z_{c-,in}$, which finally gives a measurement of the *differential position* $\delta_{diff} = \delta_+ - \delta_-$. It can be proved that differential sensing improves the sensitivity and the linearity of the sensor's output, even though the original variations of the measurand are not linear [21].

As a result of the variations of both the air gap δ and temperature T, the output voltage $U_{br,out}$ is finally an attenuated and phase-shifted version of the excitation voltage U_{exc}. More specifically, the variable air gap $\delta_{diff}(t)$ *modulates in amplitude and phase* $U_{br,out}$. Therefore, in order to recover $\delta_{diff}(t)$ and simultaneously gain full information (real and imaginary parts) on $U_{br,out}$ (and hence on the impedance Z_{diff}) *quadrature demodulation* is used. In case only $\delta_{diff}(t)$ is of interest, with e.g. minimal influence of T, it is sufficient to use only one demodulation channel.

B. ANALYSIS AND SELECTION OF THE AC WHEATSTONE BRIDGE CONFIGURATION

The AC Wheatstone bridge can be configured in many different ways: for example, the two excitation coils can be placed either in the same bridge leg or in two different legs. Additionally, it is possible to add a capacitor C_{res} in series to the excitation coil to compensate its inductive reactance at a specific resonant frequency. In this case, it would also be possible to excite the bridge with a square wave voltage, which is much simpler to realize in practice.

Three configurations of most interest are analyzed. In configuration **B1** Fig. 10(a.i), the two excitation coils make part of two different bridge legs. This is the most basic configuration, and the value of the bridge resistors R_{br} is optimized to yield the largest magnitude of $U_{br,out}$. In configuration **B2** Fig. 10(b.i), a capacitor C_{res} is added in series to each coil, and chosen to resonate with the value of $L_{c,in}$ for $\delta = 1$ mm, which is the nominal air gap. The resonant frequency is also optimized, together with the value of R_{br}, to yield the largest magnitude of $U_{br,out}$. Finally, configuration **B3** (Fig. 10(c.i)) is a variant of **B2** realized with only one capacitor in series with both bridge legs. Bridge configurations where both the excitation coils are in the same leg were studied as well, but provide in general slightly worse sensitivity to δ_{diff}, hence they are not reported. In order to select the most appropriate bridge circuit, together with the corresponding optimal excitation frequency f_{opt}, each configuration is investigated analytically. By simple AC circuital analysis, the transfer function $G(s)$ from the input voltage U_{exc} to the output voltage $U_{br,out}$ is derived. With this, it is possible to obtain $U_{br,out} = G(s)\,U_{exc}$ as a

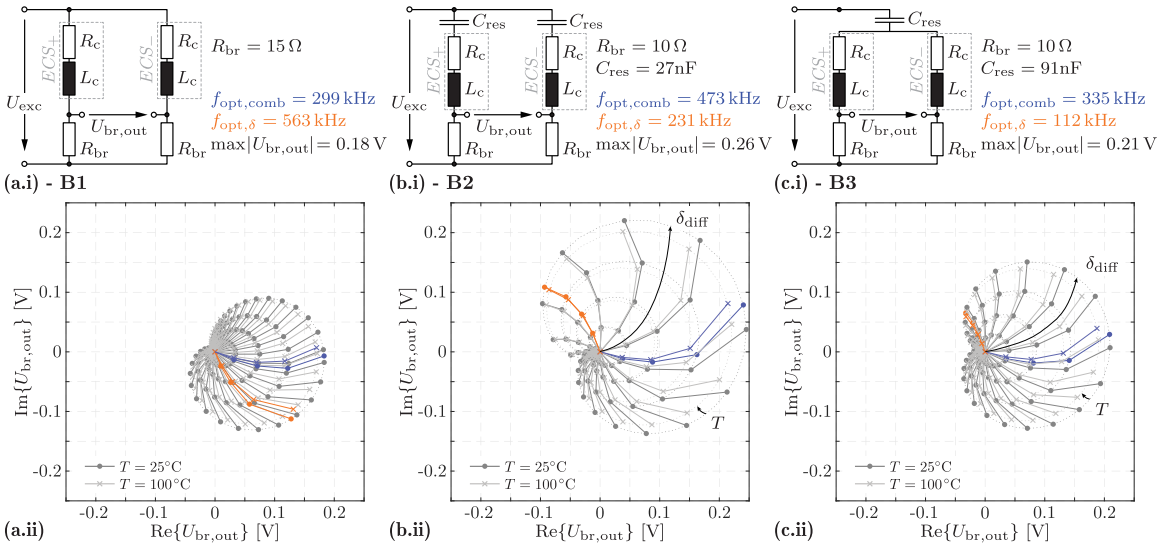

FIGURE 10. **Analysis of three differential AC Wheatstone bridge configurations with (a.i) no resonant series capacitor, (b.i) a series resonant capacitor per coil and (c.i) only one series resonant capacitor shared for the two coils. For each case, the bridge output voltage phasor $U_{br,out}$ resulting for a unitary U_{exc} is visualized on the complex plane in (a.ii), (b.ii) and (c.ii). $U_{br,out}$ is calculated for values of $f = 2\pi\omega$ logarithmically evenly spaced between 100 Hz and 10 MHz with 40 points per decade, $\delta_{diff} = \{0, 0.25, 0.5, 0.75, 1\}$ mm and $T = 25°C$ and 100°C. In order to improve visibility, only positive values of δ_{diff} are shown, as all curves are symmetric with respect to the origin. The indicated values of R_{br} and C_{res} are optimized to yield the largest magnitude of $U_{br,out}$. The highlighted curves correspond to the optimal excitation frequencies $f_{opt,comb}$ (combined δ_{diff} and T sensitivity) and $f_{opt,\delta}$ (least influence of T on δ_{diff} sensitivity) identified in Fig. 11.**

complex-valued phasor for a given array of frequencies and differential positions, starting from the measured impedance of the realized PCB-embedded coil. The influence of temperature discussed in Section IV can also be easily included in this analysis. The values of $R_{c,in}$ and $L_{c,in}$ used are the ones measured for the most sensitive shield/target combination, i.e. 0.2 mm thick stainless steel shield and 0.5 mm thick aluminum target. In Fig. 10, for each bridge configuration, $U_{br,out}$ is visualized on the complex plane for different frequencies, values of the differential position δ_{diff} and temperatures $T = 25°C$ and 100°C.

The studied configurations are compared according to a few selection criteria. The most important requirement is high sensitivity to the differential position δ_{diff}, which translates in the largest magnitude of the phasor $U_{br,out}$. The second aspect to take into consideration is the sensitivity to the temperature T. As mentioned, the designer can choose whether measuring T is of interest, or whether it is more important to minimize its influence on the δ_{diff} measurement. The normalized sensitivity curves in Fig. 11 are extracted from the data in Fig. 10 for the exemplary configuration **B1**. The δ_{diff}-sensitivity curve is given by the magnitude of $U_{br,out}$ for the largest $\delta_{diff} = 1$ mm versus frequency and normalized to its maximum. For the T-sensitivity curve, instead, the magnitude of the difference vector $U_{br,out,100°C} - U_{br,out,25°C}$ versus frequency is considered, again for $\delta_{diff} = 1$ mm and normalized to its maximum. With the sensitivity curves two optimal frequencies can be identified, for two scenarios:

1) in case *combined sensitivity* to δ_{diff} *and* T is desired, the optimal frequency $f_{opt,comb}$ can be found, which corresponds to the peak of the product sensitivity curve shown in Fig. 11, which in case of configuration **B1** leads to an optimal frequency $f_{opt,comb} = 299$ kHz. The corresponding $U_{br,out}$ obtained at this frequency on the complex plane is highlighted in blue in Fig. 10(a.ii).
2) in case only δ_{diff} is of interest, it is possible to select the frequency $f_{opt,\delta}$, which offers the optimal compromise between sensitivity to δ_{diff} and to T. This corresponds to the condition for which the sensitivity to δ_{diff} dominates the most with respect to the sensitivity T, i.e. to the peak of the ratio sensitivity curve as shown in Fig. 11. In case of configuration **B1** this leads to an optimal excitation frequency $f_{opt,\delta} = 563$ kHz. The corresponding $U_{br,out}$ obtained at this frequency on the complex plane is highlighted in orange in Fig. 10(a.ii).

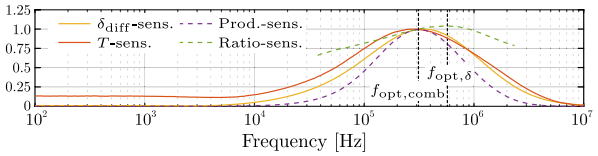

FIGURE 11. **Sensitivity curves extracted from the data of Fig. 10 for the configuration B1. Each curve is normalized to its maximum. With the product curve and the ratio curve it is possible to identify the optimal excitation frequencies for combined or δ_{diff}-only sensitivity. The ratio curve is calculated only for values of the δ_{diff}-sensitivity curve > 0.25.**

Besides sensitivity, another important requirement is the measurement bandwidth of the sensor, which has to be sufficiently high. This is directly related (approx. one decade before) to the selected f_{exc}. Finally, linearity has the least priority, as the non-linear sensor readout can eventually be corrected (e.g. in firmware).

With the results of Fig. 10, the analyzed bridge configurations can be compared and some trade-offs outlined. The sensitivity to δ_{diff} is higher for the alternatives with a resonant capacitor C_{res}. For **B2** (max $0.26\,\text{Vmm}^{-1}$) it is up to 40 % larger than **B1**. The enhanced sensitivity comes at the cost of a visibly higher non-linearity. For **B3**, instead, it is only 20 % larger than **B1**. As mentioned, the value of C_{res} is optimized together with the resonant frequency to yield the largest possible $U_{\text{br,out}}$. Interestingly, during the analysis it was found that resonance yields a sensitivity above $0.2\,\text{Vmm}^{-1}$ for a large range of frequencies, from 100 kHz to 1.4 MHz for **B2** and from 150 kHz to 600 kHz for **B3**. Therefore, these configurations give the freedom of adjusting f_{exc} according to the designer's preferences, also allowing to obtain larger bandwidths. Nevertheless, in **B2** the two resonant capacitors have to be precisely matched for good results, which can be impaired by the components' tolerances and that would require cumbersome capacitive trimming. In this sense, the advantage of **B1** is that no additional component is required. Furthermore, this simple configuration still offers a sensitivity comparable to e.g. **B3** and it allows to use higher excitation frequencies.

C. AMPLIFICATION AND DEMODULATION STAGE

Before processing $U_{\text{br,out}}$ further, a difference amplifier is employed at the output of the bridge. Typically an instrumentation amplifier is used, due to its high input impedance and common mode rejection ratio. The amplified signal is then demodulated with *coherent demodulation*, in order to preserve information on its sign. Coherent demodulation is realized by multiplying $U_{\text{br,out}}$ with the excitation signal U_{exc} (the carrier). Finally, the resulting $2 \cdot f_{\text{exc}}$ components in the multiplied signal are removed by a low-pass filter $H(s)$, with a cutoff frequency chosen e.g. a decade before f_{exc}. This way, only the low frequency information about $\delta_{\text{diff}}(t)$ is retained. Importantly, provided that all the previous stages are designed to achieve a sufficiently high bandwidth (e.g. at least one decade larger than f_{exc}), the final measurement bandwidth of the ECS is only defined by the cutoff frequency of the low-pass filter. Quadrature demodulation is realized with an additional channel, which employs a 90° phase-shifted version of the carrier. With the combined information from the *in-phase* (I-) and *quadrature* (Q-) channels, the modulating signal can be fully recovered. In fact, it can be easily verified that the I- and Q- voltages U_I and U_Q correspond to the real and imaginary components of the complex phasor $U_{\text{br,out}}$ scaled by a factor 0.5 and hence

$$\delta_{\text{diff}}(t) \propto \left|U_{\text{br,out}}\right|(t) = 2\sqrt{U_I^2(t) + U_Q^2(t)}. \qquad (17)$$

Finally, the demodulated U_I and U_Q are the signals that have to be measured or sampled by an ADC. If the gain of the instrumentation amplifier is adjusted to fully utilize the input range of the ADC, the final resolution of the ECS is defined by the number of bits of the ADC. Clearly, bridge configurations that offer a large sensitivity will result in a better signal-to-noise ratio.

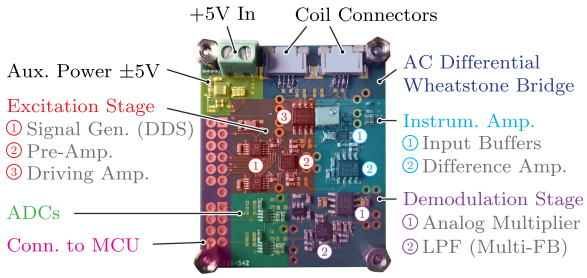

FIGURE 12. Realized PCB prototype of the measurement/evaluation board. The board is provided with a single $U_{\text{DC}} = 5\text{V}$ power supply, from which a dual ±5V power supply is generated by the auxiliary power stage (*LMZ21701* and *TPS63700, Texas Instruments*). The excitation stage uses a *LTC6227* (*Analog Devices*) for pre-amplification and a *THS4211* (*Texas Instruments*) to drive the coils. The instrumentation amplifier is realized with two *LTC6228* as input buffers and a *AD8099* for the difference amplifier (very good CMRR, −105 dB up to 1 MHz). The demodulation stage uses the *AD835* (*Analog Devices*) four-quadrant analog multiplier and another *LTC6227* for the active lowpass filer.

D. REALIZED MEASUREMENT/EVALUATION BOARD

The proposed measurement circuit is implemented with a hardware evaluation board prototype, shown in Fig. 12. The excitation stage consists of a stimulus generator followed by a driving stage, which can supply the bridge with sufficient current. In order to allow for the maximum flexibility during commissioning of the ECS, the stimulus generator is the Direct Digital Synthesizer *AD9833* by *Analog Devices*. This IC is very simple to use and it can be programmed via SPI to generate sine, square or triangular voltage waveforms with frequencies up to 12.5 MHz and a resolution of 0.1 Hz. The generated signal is pre-processed with a *RC* high-pass filter (15 Hz cutoff) for DC removal, and then pre-amplified to an amplitude of 1V, which matches the input specifications of the analog multiplier. In fact, this is the signal used later as demodulation carrier. The 90° phase-shifted carrier for the Q-channel is also generated exactly in the same way, with a second *AD9833*. The driving amplifier is configured with a gain of 2.5, thus outputting the excitation voltage U_{exc} with an amplitude of 2.5V. The AC differential Wheatstone bridge follows, implemented in such a way that all the possible bridge configurations (cf. Fig. 10) can be realized. Although monolithic solutions exist, the instrumentation amplifier is realized with three op-amps in order to guarantee high bandwidth (above 10 MHz). The gain of the instrumentation amplifier is adjustable with a 2 kΩ precision trimmer resistor, in order to match the input voltage levels of the analog multiplier (±1V) for the largest $\delta_{\text{diff}} = \pm 1\,\text{mm}$. For each of the two demodulation channels, the analog multiplier takes the amplified version of $U_{\text{br,out}}$ and the pre-amplified U_{exc} as inputs. Each product signal is then filtered with an active 4th order lowpass filter in a *Multi-Feedback* configuration [22]. The chosen cutoff frequency is 30 kHz. Additionally, this stage features a gain of 2 to compensate the 0.5 factor introduced by demodulation and a 2.5 V level shift to obtain a positive output signal. This way, the two demodulated I- and Q- voltages can be sampled with the 12-bit ADC *LTC2313*, which has an input

voltage range from 0V to 4.096V. Therefore, with the gain of the instrumentation amplifier adjusted to get a ±1V output for $\delta_{\text{diff}} = \pm 1$ mm, the final sensitivity is 1 mVμm^{-1}, which with the given 12-bits quantization and input range of the *LTC2313* results in a displacement resolution of 1 μm.

VI. MEASUREMENTS AND RESULTS

The impedance variations were verified with the realized PCB-embedded excitation coil in Section III for different values of the air gap δ. In this section, the proposed measurement circuit, implemented with the realized evaluation board, is verified instead.

A. MEASUREMENT CIRCUIT VERIFICATION

The functionality of the measurement circuit is verified with both *static* and *dynamic* measurements.

1) STATIC MEASUREMENTS FOR DIFFERENT TEMPERATURES

As the name suggests, the static measurements are realized for fixed values of the differential position δ_{diff}. By sweeping the excitation frequency and plotting on the complex plane the measured values of U_I and U_Q, it is possible to obtain the experimental version of the bridge output plots of Fig. 10, scaled by the constant gain of the instrumentation amplifier. Also the temperature T is varied from 25°C to 100°C. With the following set of measurements, the functionality of the measurement circuit (excitation, differential bridge configuration, demodulation) is verified completely.

First of all, multiple sample buildups are prepared as described in Section III for the differential positions $\delta_{\text{diff}} = \{0.5, 0.75, 1\}$ mm and placed in an oven with controllable temperature. They are connected through a hole in the wall of the oven to the evaluation board, which is placed outside of the oven as close as possible. For each measurement, all the sample buildups are first heated up to the desired temperature. Then, a pair of sample buildups is connected to the evaluation board and a frequency sweep from 10 kHz to 10 MHz and 40 points per decade is automatically performed. This is done by commanding the desired frequency to the signal generators and then acquiring 100 samples with both I- and Q- channels ADCs, which are then averaged. In the process, some intermediate signals, like e.g. U_{exc} and the output of the instrumentation amplifier are monitored with an oscilloscope. When the measurement is completed, the next pair of sample buildups is connected, a certain time is waited in order for their temperature to settle again to the desired value and finally the routine is restarted. The results are visualized in Fig. 13 for the prototypical case with 0.2 mm thick stainless steel shield and 0.5 mm thick aluminum target and the bridge configuration **B1**. The 2.5 V level shift introduced by the low-pass stage is removed by measuring the ADC readings for no excitation and removing such offset from the measured data. Additionally, in order to recover the original $U_{\text{br,out}}$ and allow a more direct comparison with Fig. 10(a.ii), the measurements are scaled down by the gain of instrumentation amplifier, which

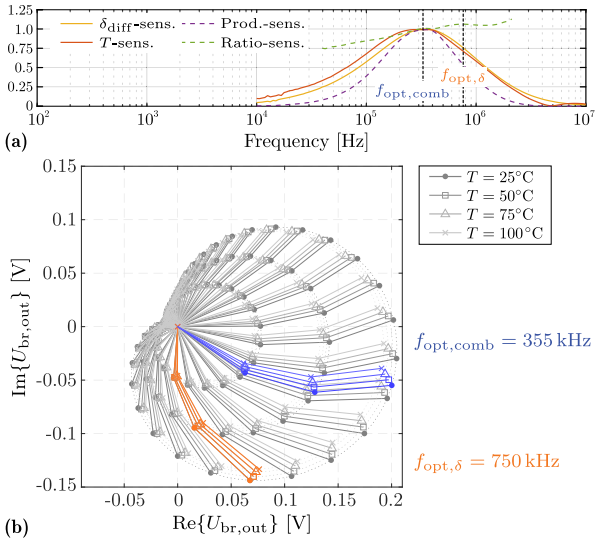

FIGURE 13. Experimental verification of the evaluation board implementing the bridge configuration B1. (a) Sensitivity curves (δ_{diff}-, T-, product and ratio) extracted from the measurements, each normalized to its maximum. The optimal excitation frequencies for combined or δ_{diff}-only sensitivity are indicated. (b) Complex plane with the sampled I- and Q-output voltages of the measurement circuit, scaled by the gain of the instrumentation amplifier to reconstruct the bridge output voltage phasor $U_{\text{br,out}}$. The measurements are performed automatically for values of $f = \omega/2\pi$ logarithmically evenly spaced between 10 kHz and 10 MHz with 40 points per decade, $\delta_{\text{diff}} = \{0.5, 0.75, 1\}$ mm and $T = \{25, 50, 75, 100\}$ °C.

is measured experimentally for a test excitation and is equal to $G_{\text{InA}} = 1.5\,\text{V/V}$ in this case, and by a factor 2.5 because of the ± 2.5 V U_{exc}. Fig. 13(a) shows the sensitivity curves introduced in Fig. 11, which are extracted from the measured data plotted on the complex plane in Fig. 13(b). The optimal excitation frequency $f_{\text{opt,comb}} = 355\,\text{kHz}$ is close to the expected value of 299 kHz. However, $f_{\text{opt},\delta} = 750\,\text{kHz}$ is about 33 % off. This can be explained by the fact that the ratio-sensitivity curve in Fig. 13(a) is relatively flat, and hence its maximum can deviate strongly from the predicted one in Fig. 11. Also the temperature's influence is visible and measurable if two demodulation channels are used. With the additional points for 50°C and 75°C, it can also be verified that the voltage varies smoothly within the two boundary curves.

2) DYNAMIC MEASUREMENTS AND BANDWIDTH VERIFICATION

As a final step, the measurement bandwidth of the realized ECS is verified with an experimental Bode plot. As mentioned, the low-pass filter of the demodulation stage is the one defining the final ECS bandwidth. For this reason, this verification can be conducted electrically with a signal generator. In particular, the $U_{\text{br,out}}$ resulting from a target moving sinusoidally can be emulated by a sinusoidal carrier at the frequency f_{exc} with double-sideband amplitude modulation (DSB-AM). The carrier's frequency is fixed to $f_{\text{exc}} = 300\,\text{kHz}$ and its amplitude is 0.4V, chosen together with the gain of the instrumentation amplifier $G_{\text{InA}} = 2.5\,\text{V/V}$ to get a ±1V output. The frequency of the modulating sine wave is swept from

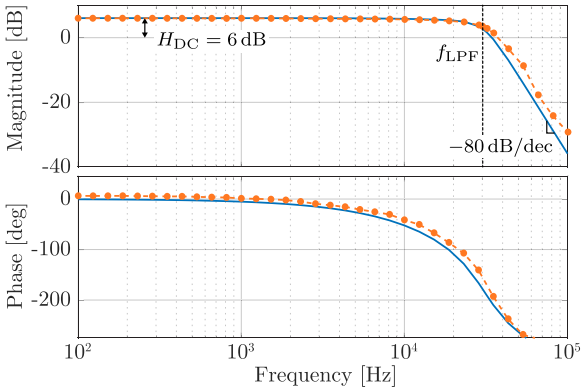

FIGURE 14. Experimental Bode plot verifying the transfer function $H(s)$ of the low-pass stage used after the analog multiplier for amplitude demodulation. The blue line is obtained from the analytic transfer function. The measurements confirm the expected DC gain, cutoff frequency and a fourth-order low-pass characteristic.

100 Hz to 100 kHz with 11 points per decade. The ±1V carrier used for demodulation by the multiplier is provided by the same external generator, in order to guarantee synchronization between the signals. The output of the low-pass filter is a sine wave with the same frequency as the modulating signal, as expected. For each frequency, its amplitude is measured (which, compared to the unitary voltage input directly gives the gain of $H(s)$), together with the phase-shift with respect to the DSB-AM modulating signal. Fig. 14 shows the obtained experimental Bode plot. The analytic transfer function for the Multi-Feedback active filter configuration is given in [22]. Two of such second-order filter stages are cascaded, with the values of the passive components selected to yield a DC gain $H_{DC} = 6\,\text{dB}$, a cutoff frequency of $f_{LPF} = 30\,\text{kHz}$ and an overall fourth-order low-pass characteristic with −80 dB slope beyond f_{LPF}. All these characteristics are verified by the measurements. Consequently, the final ECS measurement bandwidth lies approx. one decade before f_{LPF}, i.e. $f_{ECS} \approx 3\,\text{kHz}$.

VII. CONCLUSION

This paper discusses the design of an eddy current sensor (ECS) measuring the position of a moving conductive target located behind another fixed conductive shield. The analysis previously started with the aid of FEM simulations in [10] is now extended and completed with a full analytical transformer model, which describes the impedance variations of the sensor's excitation coil for varying frequency and air gap and allows to calculate the optimal excitation frequencies, thus allowing to design optimally the excitation coil to maximize e.g. position sensitivity. Then an investigation on the temperature's influence on the sensor's output is conducted, which is a relevant problem given the underlying application. Temperature particularly affects the resistive part of the impedance variations, so it has to be taken into account also while selecting a sensor interface. The most suitable measurement circuit is a differential AC Wheatstone bridge, which is analyzed thoroughly to find the optimal excitation frequencies which result in the maximum output voltage. Finally, a measurement setup consisting of a hardware prototype of the evaluation board, the excitation coil and various thin metallic samples is realized. The results verify the functionality of the measurement circuit, of the sensor concept itself and its achievable bandwidth. With a 30 kHz measurement bandwidth, a sensitivity of $1\,\text{mV}\mu\text{m}^{-1}$ and 1 µm resolution, the studied ECS is applicable as a highly-dynamic position measurement system for entirely sealed MBs. In future work, stable operation of AMBs using the proposed ECS can be demonstrated experimentally with a hardware prototype of a sealed actuator. In this context, the exact number of sensors required and their placement will be analyzed. Such experimental setup would also allow to investigate the impact of disturbing magnetic fields coming from the stator's winding on the proposed ECS.

APPENDIX

The expression of the excitation coil's input impedance $Z_{c,in}(\omega, \delta)$ obtained from the equivalent transformer model is reported:

$$Z_{c,in}(\omega, \delta) = \frac{Z_{NUM}(\omega, \delta)}{Z_{DEN}(\omega, \delta)} \tag{18}$$

$$\begin{aligned} Z_{NUM}(\omega, \delta) &= R_1R_2R_3 \\ &+ j\,(L_1R_2R_3 + L_2R_1R_3 + L_3R_1R_2)\,\omega + \ldots \\ &- \big(L_1L_2R_3 + L_1L_3R_2 + L_2L_3R_1 - L_1L_2R_3{k_{12}}^2 \\ &- L_1L_3R_2{k_{13}}^2 - L_2L_3R_1{k_{23}}^2\big)\,\omega^2 + \ldots \\ &- \big(L_1L_2L_3 - j\,L_1L_2L_3{k_{12}}^2 - j\,L_1L_2L_3{k_{23}}^2 \\ &- j\,L_1L_2L_3{k_{13}}^2 + 2j\,L_1L_2L_3k_{12}k_{13}k_{23}\big)\,\omega^3 \end{aligned} \tag{19}$$

$$\begin{aligned} Z_{DEN}(\omega, \delta) &= R_2R_3 + j\,(L_2R_3 + L_3R_2)\,\omega \\ &+ L_2L_3\left({k_{23}}^2 - 1\right)\omega^2 \end{aligned} \tag{20}$$

REFERENCES

[1] A. J. Fleming, "A review of nanometer resolution position sensors: Operation and performance," *Sensors Actuators A: Phys.*, vol. 190, pp. 106–126, 2013.

[2] B. George, Z. Tan, and S. Nihtianov, "Advances in capacitive, eddy current, and magnetic displacement sensors and corresponding interfaces," *IEEE Trans. Ind. Electron.*, vol. 64, no. 12, pp. 9595–9607, Dec. 2017.

[3] J. Boehm, R. Gerber, and N. R. C. Kiley, "Sensors for magnetic bearings," *IEEE Trans. Magn.*, vol. 29, no. 6, pp. 2962–2964, Nov. 1993.

[4] L. Xi'nan, W. Fengxiang, and W. Baoguo, "Application of eddy-current sensor for air gap detection in magnetic suspension motors," in *Proc. 5th Int. Conf. Elect. Mach. Syst.*, 2001, pp. 326–329.

[5] S. Miric, R. Giuffrida, D. Bortis, and J. Kolar, "Dynamic electromechanical model and position controller design of a new high-precision self-bearing linear actuator," *IEEE Trans. Ind. Electron.*, vol. 68, no. 1, pp. 744–755, Jan. 2021.

[6] T. Wellerdieck, "The bearingless pump for high fluid temperatures," (in German), Ph.D. dissertation, Dept. Inf. Technol. Elect. Eng., ETH Zurich, Zürich, Switzerland, 2017.

[7] A. Sophian and M. Fan, "Pulsed eddy current non-destructive testing and evaluation: A review," *Chin. J. Mech. Eng.*, vol. 30, pp. 1474–1474, Nov. 2017.

[8] S. Shokralla, S. Sullivan, J. Morelli, and T. W. Krause, "Modelling and validation of eddy current response to changes in factors affecting pressure tube to calandria tube gap measurement," *NDT&E Int.*, vol. 73, pp. 15–21, 2015.
[9] T. Baumgartner, R. M. Burkart, and J. W. Kolar, "Analysis and design of a 300-W 500000-r/min slotless self-bearing permanent-magnet motor," *IEEE Trans. Ind. Electron.*, vol. 61, no. 8, pp. 4326–4336, Aug. 2014.
[10] R. V. Giuffrida, S. Mirić, D. Bortis, and J. W. Kolar, "Looking through walls—actuator position measurement through a conductive wall," in *Proc. 23nd Int. Conf. Elect. Mach. Syst.*, 2020, pp. 1649–1654.
[11] S. S. Mohan, M. del Mar Hershenson, S. P. Boyd, and T. H. Lee, "Simple accurate expressions for planar spiral inductances," *IEEE J. Solid-State Circuits*, vol. 34, no. 10, pp. 1419–1424, Oct. 1999.
[12] J. Zhao, "A new calculation for designing multilayer planar spiral inductors," *Elect. Des. News*, vol. 55, no. 14, pp. 37–40, 2010.
[13] D. Vyroubal, "Impedance of the eddy-current displacement probe: The transformer model," *IEEE Trans. Instrum. Meas.*, vol. 53, no. 2, pp. 384–391, Apr. 2004.
[14] H. A. Wheeler, "Simple inductance formulas for radio coils," *Proc. Inst. Radio Engineers*, vol. 16, no. 10, pp. 1398–1400, 1928.
[15] C. Akyel, S. Babic, and S. Kincic, "New and fast procedures for calculating the mutual inductance of coaxial circular coils (circular coil-disk coil)," *IEEE Trans. Magn.*, vol. 38, no. 5, pp. 2367–2369, Sep. 2002.
[16] W. G. Hurley, M. C. Duffy, J. Zhang, I. Lope, B. Kunz, and W. H. Wölfle, "A unified approach to the calculation of self- and mutual-inductance for coaxial coils in air," *IEEE Trans. Power Electron.*, vol. 30, no. 11, pp. 6155–6162, Nov. 2015.
[17] M. R. Nabavi and S. N. Nihtianov, "Design strategies for eddy-current displacement sensor systems: Review and recommendations," *IEEE Sensors J.*, vol. 12, no. 12, pp. 3346–3355, Dec. 2012.
[18] P. Kejík, C. Kluser, R. Bischofberger, and R. S. Popovic, "A low-cost inductive proximity sensor for industrial applications," *Sensors Actuators, A: Phys.*, vol. 110, no. 1–3, pp. 93–97, Feb. 2004.
[19] G. Zhao, J. Yin, L. Wu, and Z. Feng, "Ultrastable and low-noise self-compensation method for circuit thermal drift of eddy current sensors based on analog multiplier," *IEEE Trans. Ind. Electron.*, vol. 67, no. 10, pp. 8851–8859, Oct. 2020.
[20] V. Chaturvedi, J. G. Vogel, K. A. Makinwa, and S. Nihtianov, "A 19.8-mW Eddy-current displacement sensor interface with sub-nanometer resolution," *IEEE J. Solid-State Circuits*, vol. 53, no. 8, pp. 2273–2283, Aug. 2018.
[21] R. Pallas-Areny and J. Webster, *Sensors and Signal Conditioning*, 2nd ed. Hoboken, NJ, USA: Wiley, 2001.
[22] J. Karki, "Active low-pass filter design," Texas Instruments, Dallas, TX, USA, Tech. Rep. SLOA049B, Sep. 2002.

ROSARIO V. GIUFFRIDA (Student Member, IEEE) received the B.Sc. degree in electronics engineering from the University of Catania, Catania, Italy, in 2016, and the M.Sc. degree in robotics, systems, and control in 2019 from the Swiss Federal Institute of Technology (ETH) Zurich, Switzerland, where he is currently working toward the Ph.D. degree in the advanced mechatronic systems area with the Power Electronic Systems Laboratory. His research interests include machine design, sensing, and motion control concepts for novel self-bearing linear-rotary actuators used in high-purity/medical applications.

SPASOJE MIRIĆ (Student Member, IEEE) received the B.Sc., M.Sc., and Ph.D. degrees in electrical engineering from the School of Electrical Engineering, University of Belgrade, Belgrade, Serbia, in 2012, 2013, and 2018, respectively, with focus on power electronics systems and drives. In 2021, he defended the second Ph.D. thesis with the Power Electronic Systems Laboratory, ETH Zurich, Zurich, Switzerland, in the advanced mechatronic systems area. During the Ph.D. project, he focused on linear-rotary actuator systems with magnetic bearings, which resulted in two new machine topologies which have been patented. Since 2021, he has been with PES as a Postdoc Researcher. His research interests include WBG power converter optimization with hard and soft-switching, new modulation techniques of flying capacitor converters, wireless power transfer systems, and eddy-current-based position sensor systems.

JOHANN W. KOLAR (Fellow, IEEE) received the M.Sc. and Ph.D. degree (*summa cum laude*) from the University of Technology Vienna, Vienna, Austria, in 1997 and 1999, respectively. Since 1984, he has been an independent Researcher and International Consultant in close collaboration with the Vienna University of Technology, in the fields of power electronics, industrial electronics and high performance drive systems. He was appointed as an Associate Professor and the Head of the Power Electronic Systems Laboratory, Swiss Federal Institute of Technology Zurich, Zurich, Switzerland, on February 1, 2001, and was promoted to the rank of Full Professor in 2004. He has proposed numerous novel converter concepts, including the Vienna Rectifier, Sparse Matrix Converter and Swiss Rectifier, spearheaded the development of x-million rpm motors, and has pioneered fully automated multi-objective power electronics design procedures. He has graduated more than 80 Ph.D. students, has authored or coauthored more than 900 journal and conference papers and four book chapters, and has filed more than 200 patents. His research interests include ultra-compact/efficient WBG converter systems, ANN-based design procedures, solid-state transformers, ultra-high speed drives, and bearingless motors. He has presented more than 30 educational seminars at leading international conferences and has served as IEEE PELS Distinguished Lecturer from 2012 to 2016. He was the recipient of more than 40 IEEE Transactions and Conference Prize Paper Awards, 2014 IEEE Power Electronics Society R. David Middlebrook Achievement Award, 2016 IEEE PEMC Council Award, 2016 IEEE William E. Newell Power Electronics Award, 2021 EPE Outstanding Achievement Award and two ETH Zurich Golden Owl Awards for excellence in teaching. He was elected to the U.S. National Academy of Engineering as an International Member in 2021.

DOMINIK BORTIS (Senior Member, IEEE) received the M.Sc. and Ph.D. degrees in electrical engineering from the Swiss Federal Institute of Technology (ETH) Zurich, Switzerland, in 2005 and 2008, respectively. In May 2005, he joined the Power Electronic Systems Laboratory (PES), ETH Zurich, as a Ph.D. student. From 2008 to 2011, he was a Postdoctoral Fellow and from 2011 to 2016 a Research Associate with PES. Since January 2016, he has been heading the Research Group Advanced Mechatronic Systems, PES, which concentrates on ultra-high speed motors, bearingless drives, linear-rotary actuator and machine concepts with integrated power electronics. He has authored or coauthored more than 90 scientific papers in international journals and conference proceedings and filed more than 30 patents. His research interests include highly dynamic positioning systems, medical systems, and future mobility concepts. He was the recipient of ten IEEE Conference Prize Paper Awards and two First Prize Transaction Paper Award.